Surface aging behaviour of Fe-based amorphous alloys as catalysts during heterogeneous photo Fenton-like process for water treatment

Z. Jia[a], J. Kang[b], W.C. Zhang[c], W.M. Wang[d], C. Yang[e], H. Sun[a], D. Habibi[a], L.C. Zhang[a],*

[a] School of Engineering, Edith Cowan University, 270 Joondalup Drive, Joondalup, Perth, WA 6027, Australia
[b] Department of Chemical Engineering, Curtin University, GPO Box U1987, Perth, WA 6845, Australia
[c] Environmental Protection Administration of Ji'an City, Ji'an, Jiangxi Province, 343000, China
[d] School of Materials Science and Engineering, Shandong University, Jinan, Shandong 250061, China
[e] National Engineering Research Center of Near-net-shape Forming for Metallic Materials, South China University of Technology, Guangzhou 510640, China

ABSTRACT

Two novel, multifunctional Fe-based amorphous alloys with the nominal components of $Fe_{78}Si_9B_{13}$ and $Fe_{73.5}Si_{13.5}B_9Cu_1Nb_3$ exhibit advanced catalytic capability when degrading methyl blue (MB) and methyl orange (MO) dyes. The production rate of hydroxyl radicals ($^{\bullet}OH$) in this work is 5–10 times faster than other Fe-based catalysts. The surface aging behaviour on $Fe_{78}Si_9B_{13}$ and $Fe_{73.5}Si_{13.5}B_9Cu_1Nb_3$ ribbons shows a significant effect on the dye degradation efficiency and reusability of the catalyst. Results reveal that crystallized α-Fe, iron oxide and SiO_2 are gradually precipitated on the surface of the reused $Fe_{78}Si_9B_{13}$ ribbon which ultimately becomes corroded through with holes. However, the inclusion of Nb atoms in the $Fe_{73.5}Si_{13.5}B_9Cu_1Nb_3$ alloy causes the formation of niobium oxides which overlay the ribbon surface, and tend to reduce the contact area between the Fe and H_2O_2, thereby decreasing the generation of $^{\bullet}OH$ and further reducing the dye degradation efficiency. Tert-butanol is employed for quenching hydroxyl radicals ($^{\bullet}OH$), causing a dramatic reduction in the amount available for degrading the MB and MO molecules. The MB and MO dye degradation and mineralization under UV–vis light are also fully investigated. The findings of this critically important work should form the basis of new research opportunities into the study of amorphous alloy catalysis.

© 2016 Elsevier B.V. All rights reserved.

1. Introduction

Metallic glasses or amorphous alloys have attracted considerable attention due to the excellent combination of desirable physical and chemical properties, such as high strength, corrosion resistance, and soft magnetic property *etc*. In addition to the functional applications, the metallic glasses have been also utilized as biomaterials [1,2], catalysts [3,4], and nanotechnology [5,6]. Largely because of their superior soft magnetic property and low cost, Fe-based metallic glasses have attracted a great deal of research attention since they are discovered. Recently, several amorphous alloys, including MgZn-based alloys [7], Co-based alloys [4], and Fe-based alloys such as Fe-Si-B [3], Fe-Mo-Si-B [8], and Fe-Si-B-Cu-Nb [9] alloys have been reported as having the potential for the

advanced catalytic capability for wastewater remediation. Each of these amorphous alloys has demonstrated ultrafast dye degradation efficiency. Due to their superior soft magnetic property and chemical stability, Fe-based metallic glasses are easy to be recycled and have an acceptable level of surface decay, which would offer dramatic cost reductions when employed as a catalyst in industrial settings. Very recently, the Fe-based metallic glasses as catalysts for wastewater remediation have been extensively reported. It is found that the acid orange II dye can be rapidly degraded by Fe-Si-B-Mo and Fe-Si-B metallic glasses [10,11]. The direct blue 6 dye degradation efficiency using Fe-B amorphous alloy is 89 and 1.8 times faster than the commercial iron powders and Fe-B crystalline alloy, respectively [12]. The reusability of the amorphous alloys is also a very attractive property when they are used as catalysts in wastewater purification [3,13,14]. The Fe-Si-B-Y powders in amorphous state present 1000 times higher reactivity than the commercial Fe powders for methyl orange degradation, the reusability of this catalysts can be achieved to 13 cycles [15]. Fe-Si-B metallic glass exhibits 30 times of reusability and a superior surface stability while activating persulfate for methyl blue (MB) degradation [16].

* Corresponding author.
E-mail addresses: l.zhang@ecu.edu.au, lczhangimr@gmail.com (L.C. Zhang).

The effect of brilliant red 3B-A dye adsorption behaviour for Fe-Si-B and Fe-Si-B-Cu-Nb amorphous alloys has also been reported [17]. The Fe-B-Y metallic glass presents a high reactivity in degrading Orange G dye due to the weak atomic bonds of amorphous atoms [18]. To date, however, the mechanisms of amorphous alloy for surface decay behaviour have rarely been reported.

Methyl blue (MB) and methyl orange (MO) are two of the typical dyes being utilized in biology and medicine, and also as a photochromophore to sensitize gelatinous films [19]. The established methods aimed at degrading dyes from industrial effluent can be divided into three groups, i.e. physical process, such as nanofiltration [20], adsorption [21], flocculation [22] and ion exchange [23], biological degradation process [24], and chemical methods including advanced oxidation processes (AOPs), such as photocatalysis [25–28], ozone (O_3) [29] and Fenton/Fenton-like method [30–32]. The Fenton method is an effective way to eliminate organic matters from waste water. In the traditional Fenton method, the iron ions/salts are particularly treated as the catalysts to activate the hydrogen peroxide for producing highly reactive transitory species such as hydroxyl radicals ($^{\bullet}OH$, $E^o = 2.7$–$2.8\,V$ [33]) for remediating toxic components in the aqueous matrix. However, the most important drawbacks to this homogeneous Fenton method are mainly due to: (1) ferric hydroxide sludge is easily produced at alkaline conditions [34]; (2) the iron ions are difficult to be recycle used [35]; (3) the cost associated with the purification of the secondary sludge and catalyst reusability may limit the actual application in the industrial scale; and (4) the produced unfavourable ferric hydroxide sludge will block the UV radiation penetration in photo-Fenton method [35]. Very recently, in order to overcome the shortcomings of the homogeneous Fenton catalysts, various sized particles of zero valent iron (ZVI) are employed as effective catalysts, commonly either in granular form, or in a powder form, or as nano-scaled particles. A high specific surface area is able to enhance oxidation during the Fenton process, which in turn accelerates the dye decolorization rate. However, as dye wastewater is usually of high temperature, the oxidative capability of ZVI is very constrained. Moreover, the ZVI would lose reactivity once the active sites of ZVI are occupied by oxidants. In newer methods, the amorphous alloys demonstrate a superior catalytic property for wastewater remediation in comparison to ZVI. These merits are mainly attributed to their soft magnetic property, excellent corrosion resistance and the unique metastable thermodynamic nature.

This work is comprised of a comprehensive study of the reusability and surface decay mechanisms of both $Fe_{78}Si_9B_{13}$ and $Fe_{73.5}Si_{13.5}B_9Cu_1Nb_3$ metallic glasses, which are used as catalysts under the heterogeneous photo-Fenton-like process for dye wastewater treatment. The MB and MO dye decolorization, mineralization and reaction kinetics (k) using amorphous $Fe_{78}Si_9B_{13}$ and $Fe_{73.5}Si_{13.5}B_9Cu_1Nb_3$ alloys are investigated in detail. The surface decay evolution of $Fe_{78}Si_9B_{13}$ and $Fe_{73.5}Si_{13.5}B_9Cu_1Nb_3$ are also thoroughly studied. The effect of the inclusion of Nb atoms in $Fe_{73.5}Si_{13.5}B_9Cu_1Nb_3$ amorphous alloy is also presented in detail.

2. Materials and methods

Amorphous alloy ribbons of 30–40 μm thickness having the nominal composition of $Fe_{78}Si_9B_{13}$ and $Fe_{73.5}Si_{13.5}B_9Cu_1Nb_3$ in atomic percentages were prepared by vacuum melt-spinning [36,37]. The MB and MO dyes used throughout this study were supplied by Xilong Chemical Co., Ltd (China). The chemicals such as H_2O_2 (30 wt.%), Milli-Q water (18.2 MΩ·cm), $NaNO_2$ (0.5 M), benzoic acid (200 ppm), tert-butanol, NaOH (0.1 M) and HCl (0.1 M) were all of the analytical grades. The structural characterizations of the $Fe_{78}Si_9B_{13}$ and $Fe_{73.5}Si_{13.5}B_9Cu_1Nb_3$ amorphous ribbons before and after degradation were examined by use of XRD with Co-Kα

radiation (PANalytical Empyrean, Netherlands) and UV–vis DRS (Shelton, CT, USA). The SEM equipped with EDS (JEOL 6000, Japan) was used for the investigation of surface morphology of the ribbons. The ultrasonic cleaner was firstly used for cleaning the recycled ribbons in Milli-Q water, after which the surface was further washed by alcohol.

Dye degradation experiments were conducted in a beaker (200 ml) vibrating in a Vortex-Genie 2 mixer (Scientific Industries, Inc. USA) throughout the dye degradation progress under a 300 W simulated solar light (Perfectlight Scientific Pty Ltd, Beijing, China). A fixed 0.5 g/L dosage of 5×20 mm amorphous alloy ribbons was used as catalysts for the dye degradation. A specific concentration of H_2O_2 was added into the dye aqueous as the beginning of the dye degradation experiments. The irradiation distance between the light and dye aqueous solution was set to 7 cm. Water specimens were sampled at predetermined time intervals. Sodium nitrite ($NaNO_2$) with the same concentration of H_2O_2 was employed to prevent further reaction. All the samples were processed in an ultrasonic cleaner for 90 s and further filtered with a 0.45 μm Pall Corporation (New York, USA) filter. After which the sampled dye solution was measured in turn in a UV–vis spectrometer (Shelton, CT, USA) and also analyzed by a TOC-5000CE analyzer (Shimadzu, Japan) for the mineralization analysis. For Fe leaching experiment, the sample solutions were diluted 10 times with 2% w/w nitric acid (HNO_3) and then filtered by the 0.45 μm filter before the ICP-OES test (Optima 8300 ICP-OES Spectrometer, PerkinElmer). The wavelength of light absorbance λ_{max} of MB was measured to be 664 nm and of MO dye at pH value 2–3.4 (red) and 5.6–12 (yellow) was measured to be 498 and 464 nm, respectively.

3. Results and discussions
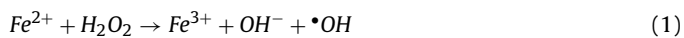
3.1. Dye degradation and mineralization

3.1.1. Methyl blue and methyl orange

The photo-Fenton-like MB (Fig. 1) and MO (Fig. 2) degradation of $Fe_{78}Si_9B_{13}$ and $Fe_{73.5}Si_{13.5}B_9Cu_1Nb_3$ are strongly influenced by pH, H_2O_2 concentration and light intensity. It is well accepted that hydroxyl radicals ($^{\bullet}OH$) having extremely high redox potential ($E^o = 2.7$–$2.8\,V$ [33]) play a key role for dye degradation. As shown in Fig. 1(a) and Fig. 2(a), the MB and MO color removals increase significantly when changing the pH from alkaline to acidic conditions. Such improved performance under acidic conditions is mainly attributed to the fast generation of hydroxyl radicals ($^{\bullet}OH$) from the reaction between Fe and H_2O_2, ensuring that an adequate number of $^{\bullet}OH$ are presented to degrade the dye molecules [3]. In contrast, when the pH value increases, representing a more alkaline condition, a large amount of Fe in the amorphous ribbons is lost to ferrous or ferric hydroxide sedimentation. This sedimentation also tends to overlay the ribbon surface and reduces the contact area between the Fe and H_2O_2. The investigation shows that inhibiting the $^{\bullet}OH$ generation would cause a profound effect on the dye degradation efficiency. Fig. 1(b) and Fig. 2(b) presents the effect of H_2O_2 concentration on MB and MO dye color removal. It can be seen that increasing H_2O_2 concentration from 0.5 mM to 2.0 mM in the presence of $Fe_{78}Si_9B_{13}$ and $Fe_{73.5}Si_{13.5}B_9Cu_1Nb_3$ greatly enhances the dye color removal rate, however, only H_2O_2 cannot effectively degrade dye molecules. This improvement arises as a result of the $^{\bullet}OH$ having an extremely high oxidation potential, which is promoted between the Fe^{2+} and H_2O_2 reaction (Eq. (1)). However, it is observed that any further increase in H_2O_2 from 1.0 mM to 2.0 mM only causes a slight improvement of the dye color removal. The excess H_2O_2 is regarded as a scavenger of $^{\bullet}OH$, converting them to penetrative $HO_2^{\bullet}$ radicals with a lower oxidation potential (Eq. (2)). The effect of light intensity on MB
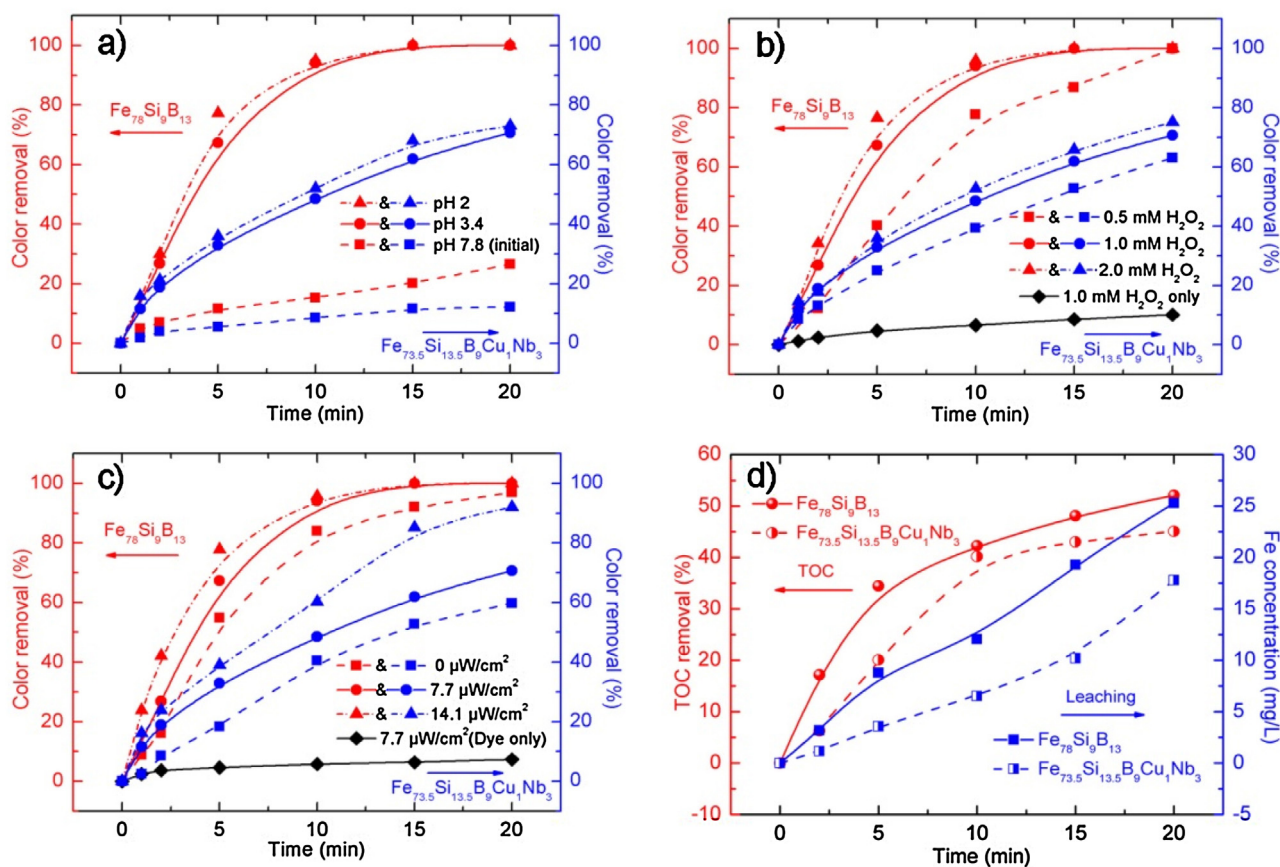
Fig. 1. Comparable results of color removals for of MB dye by using $Fe_{78}Si_9B_{13}$ and $Fe_{73.5}Si_{13.5}B_9Cu_1Nb_3$ ribbons as a function of (a) pH, (b) H_2O_2 concentration, (c) light intensity and (d) TOC removals and Fe leaching concentrations (if not mentioned, the conditions are catalyst dosage: 0.5 g/L, irradiation intensity: 7.7 μW/cm², dye concentration: 20 ppm, and H_2O_2 concentration: 1.0 mM).

and MO degradation by using $Fe_{78}Si_9B_{13}$ and $Fe_{73.5}Si_{13.5}B_9Cu_1Nb_3$ are shown in Fig. 1(c) and Fig. 2(c). Notably, both MB and MO dye degradation rates are remarkably enhanced under light irradiation. Such performance can be concluded as: 1) increasing the light irradiation intensity enhances the photo-chemical conversion causing the Fe^{2+} being regenerated from Fe^{3+} (Eq. (3)) for providing more •OH, the similar result is observed in our previous work [3]. 2) The electrons ($2e^-$) at $4S^2$ orbital around amorphous Fe atoms are unstable and easy to be activated by UV–vis light energy (Eq. (4)), providing more Fe^{2+} to react with H_2O_2. To further analyze the mineralization of MB and MO, the TOC removals by using $Fe_{78}Si_9B_{13}$ and $Fe_{73.5}Si_{13.5}B_9Cu_1Nb_3$ are shown in Fig. 1(d) and Fig. 2(d), respectively. During the dye degradation and mineralization, chromophore bond is firstly attacked by the produced •OH to cause a fast dye color removal. Afterward, the by-products are generated and further mineralized to final products as H_2O, CO_2, NO_3^-, and SO_4^{2-} thereby requiring a longer performance for complete mineralization. In addition, as seen from Fig. 1(d) and Fig. 2(d), there is no significant leaching of Fe ions (Fe^{2+} or Fe^{3+}) for both $Fe_{78}Si_9B_{13}$ and $Fe_{73.5}Si_{13.5}B_9Cu_1Nb_3$ catalysts during the degradation of MB and MO dyes. Such performance indicates the advanced surface stability of both catalysts and further evidences the superiority of these two catalysts in wastewater treatment. The details for surface stability will be presented in Section 3.2.

$$Fe^{2+} + H_2O_2 \rightarrow Fe^{3+} + OH^- + {}^\bullet OH \tag{1}$$

$${}^\bullet OH + H_2O_2 \rightarrow HO_2{}^\bullet + H_2O \tag{2}$$

$$Fe(OH)^{2+} + h\nu \rightarrow {}^\bullet OH + Fe^{2+} \tag{3}$$

$$Fe^0 \overset{h\nu}{\rightarrow} Fe^{2+} + 2e^- \tag{4}$$

The value of reaction rate (k) reflects the dye degradation efficiency. The comparable results using the two Fe-based catalysts are summarized in Table 1. The equation of the kinetic model is shown in Eq. (5):

$$ln(C_0/C) = k_{obs}t \tag{5}$$

where k_{obs} is the kinetic rate constant; C_0 is the original concentration of dye; C is the dye concentration at time t.

Compared to micro-ZVI, the amorphous $Fe_{78}Si_9B_{13}$ and $Fe_{73.5}Si_{13.5}B_9Cu_1Nb_3$ ribbons exhibit faster dye degradation rate at rational parameter control. Notably, NZVI having high reaction rates (k) of 0.199 min⁻¹ [38] and 0.559 min⁻¹ [39] is a superior candidate for rapid acid black 24 and methyl orange dye degradation. Compared to the ribbons, the higher performance of NZVI is owing to the large specific surface area being provided more active sites for producing •OH. However, the manufacturing process of micro- or nano- powders sharply increases the cost of catalysts. On the other hand, the powder catalyst is difficult to maintain high reusability since the active sites are easy to be occupied by oxidants after using one time [40]. Therefore, the amorphous alloy not only has rapid reaction rates, but also is possible to tune the chemical composition for further improving the reusability. The inclusion of various elements would significantly enhance the surface stability thereby improving the reusability (details present in Section 3.2)

3.1.2. Hydroxyl radical

Fig. 3(a) and (b) present the UV–vis spectra of MB (pH 3.4) and MO (pH 3.4) dye degradation by use of $Fe_{78}Si_9B_{13}$ and
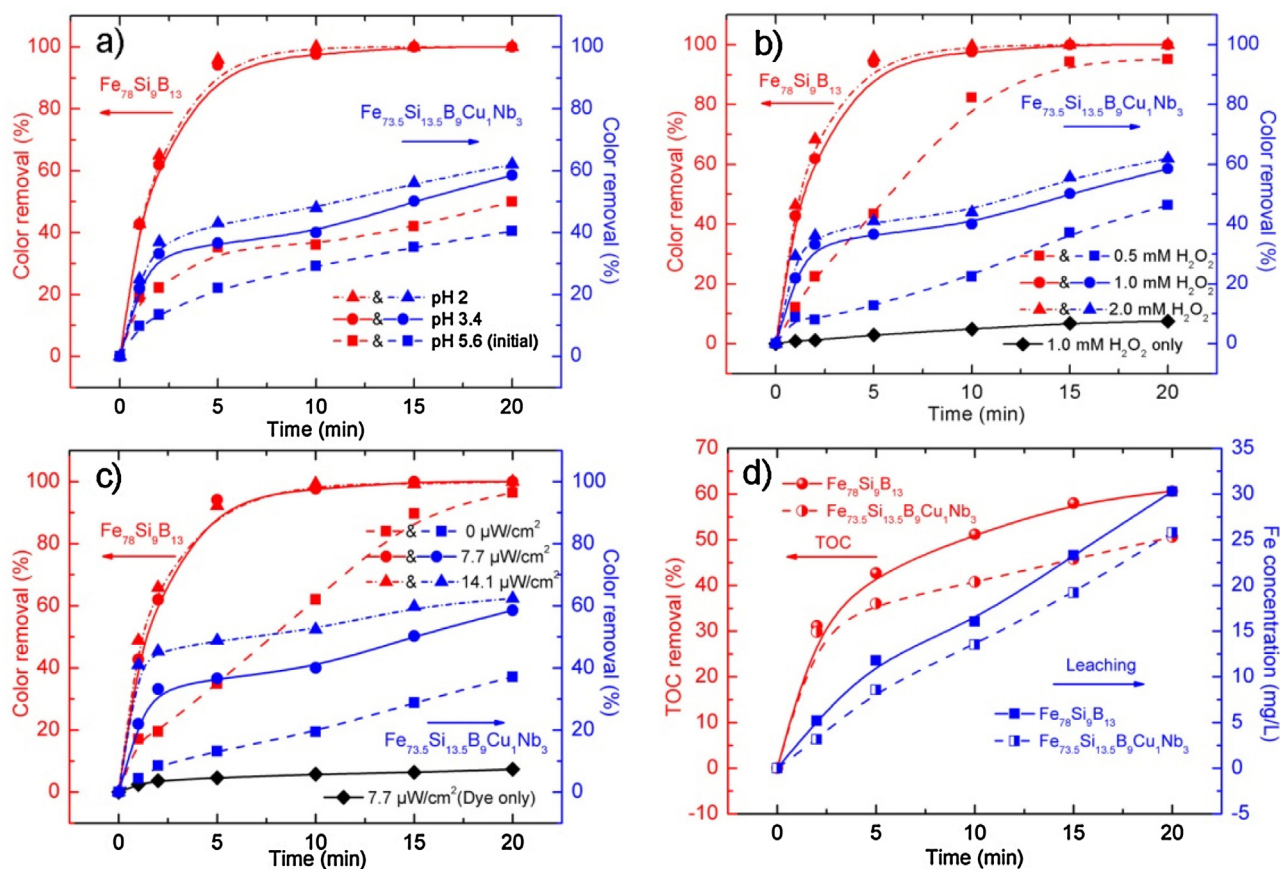
Fig. 2. Comparable results of color removals for MO dye by using $Fe_{78}Si_9B_{13}$ and $Fe_{73.5}Si_{13.5}B_9Cu_1Nb_3$ ribbons as a function of (a) pH, (b) H_2O_2 concentration, (c) light intensity and (d) TOC removals and Fe leaching concentrations (if not mentioned, the conditions are catalyst dosage: 0.5 g/L, irradiation intensity: 7.7 $\mu W/cm^2$, dye concentration: 20 ppm, and H_2O_2 concentration: 1.0 mM).

Table 1
Comparable result of reaction rates (k) by using various Fe-based catalysts in Fenton method.

Material	Dosage (g/L)	Area dosage (m^2/L)[a]	Dye	pH	Light intensity ($\mu W/cm^2$)	k_{obs} (min^{-1})	k_{SA} ($L/m^2 \cdot min$)[b]	Ref.
Micro-ZVI	200	1.42	Orange II	7.0	–	0.380	0.268	[41]
	200	1.42	Crocein Orange G	7.0	–	0.380	0.268	[41]
Micro-ZVI	66.6	–	Orange II	3.0	–	0.032	–	[42]
NZVI	0.165	23.2	Acid black 24	6.7	–	0.199	0.009	[38]
NZVI	0.5	>23.2	Methyl orange	4.0	–	0.559	<0.022	[39]
Crystal $Fe_{84}B_{16}$	0.2	0.112	Direct blue 6	7.0	–	0.052	0.554	[12]
Amorphous $Fe_{84}B_{16}$	0.2	0.112	Direct blue 6	7.0	–	0.110	0.982	[12]
Amorphous $Fe_{78}(Si,B)_{22}$	9–12	0.062	Orange II	6.0	–	0.125	2.0	[11]
Amorphous $Fe_{78}Si_9B_{13}$	0.5	0.06	Methyl orange	3.4	7.7	0.386	6.43	This work
	0.5	0.06	Methyl blue	3.4	7.7	0.381	6.35	This work
Amorphous $Fe_{73.5}Si_{13.5}B_9Cu_1Nb_3$	0.5	0.06	Methyl orange	3.4	7.7	0.152	2.53	This work
	0.5	0.06	Methyl blue	3.4	7.7	0.201	3.35	This work

[a] Area dosage is calculated by $\rho = S/V$, S is the surface area of ribbon; V is the volume of the dye aqueous solution.

[b] k_{SA} is calculated from k_{obs} by dividing ρ, reflecting the essential degradation ability.

$Fe_{73.5}Si_{13.5}B_9Cu_1Nb_3$ ribbons at various time intervals, respectively. As seen from Fig. 3(a), the maximum absorbance peaks of MB dye at $\lambda = 292$ nm and $\lambda = 664$ nm indicate the triazine group ($\pi - \pi^*$ transition) and heteropoly aromatic linkage (including chromophore and auxochrome ($-CH_3$)), respectively. Notably, these two peaks are gradually invisible with increasing the irradiation time for both $Fe_{78}Si_9B_{13}$ and $Fe_{73.5}Si_{13.5}B_9Cu_1Nb_3$ ribbons, indicating the complete dye degradation. The maximum absorbance peaks at $\lambda = 280$ nm and $\lambda = 498$ nm (Fig. 3(b)) presenting the benzenesulfonic group and N,N-dimethylaniline group in MO dye are also gradually decreased along with increasing the irradiation time. The rapid decolorization of the MB and MO dyes suggests that both

$Fe_{78}Si_9B_{13}$ and $Fe_{73.5}Si_{13.5}B_9Cu_1Nb_3$ ribbons are able to very rapidly generate hydroxyl radicals ($^\bullet OH$), resulting in the rapid cleaving of the chromophore in the MB and MO dyes. In addition, as seen from the insets of Fig. 3(a) and (b), the MB and MO degradation rate of $Fe_{78}Si_9B_{13}$ ribbon is faster than for $Fe_{73.5}Si_{13.5}B_9Cu_1Nb_3$ ribbon. It is postulated that the precipitations observed on the ribbon surface during the dye degradation have a significant effect on the efficiency of dye color removal.

Fig. 3(c) shows the changes of reaction rates (k) by using $Fe_{78}Si_9B_{13}$ and $Fe_{73.5}Si_{13.5}B_9Cu_1Nb_3$ ribbons in quenching tests. It is observed that the reaction rates (k) of both $Fe_{78}Si_9B_{13}$ and $Fe_{73.5}Si_{13.5}B_9Cu_1Nb_3$ decrease sharply after adding tert-butanol.
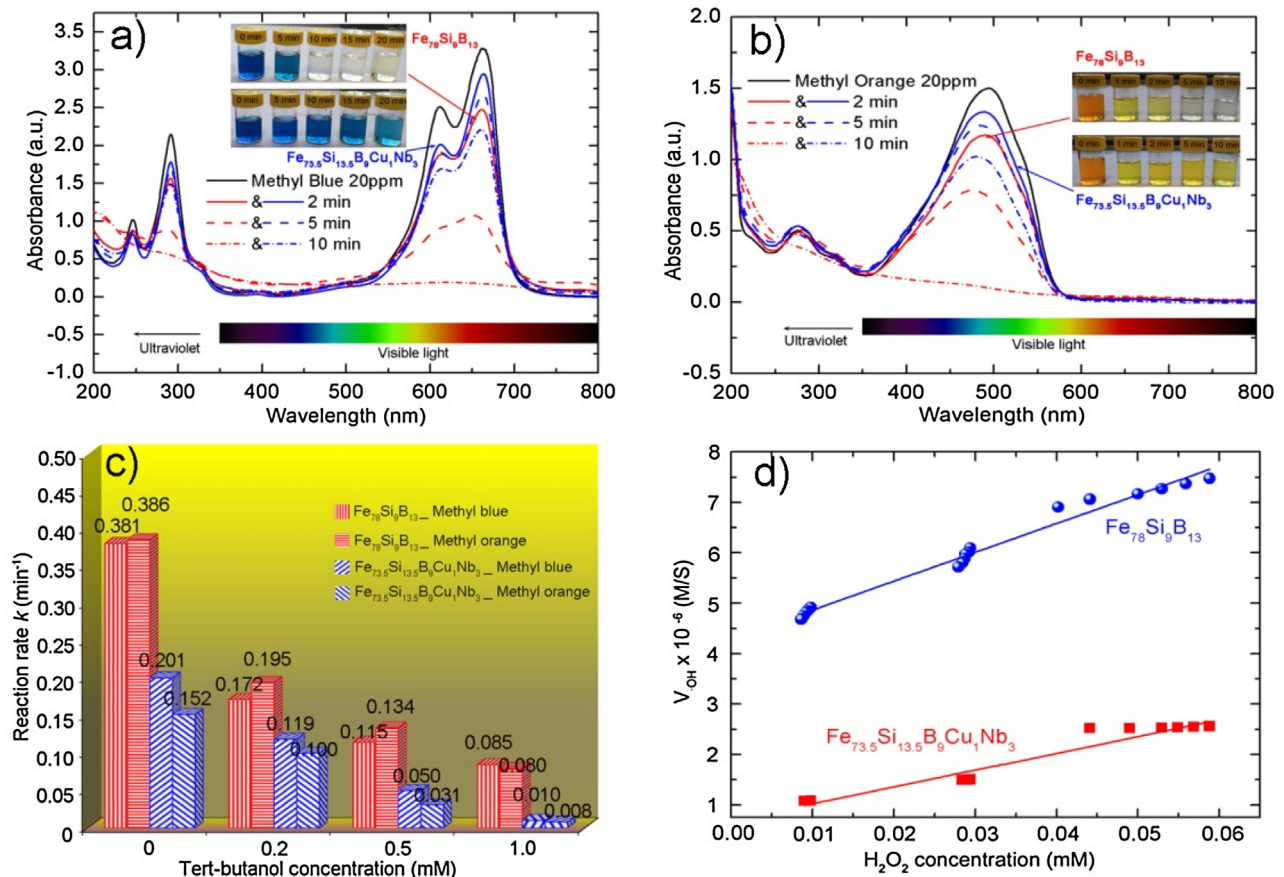
Fig. 3. UV–vis spectra of (a) MB and (b) MO color removals within different time intervals, (c) effect of *tert*-butanol concentration on MB and MO dye degradation reaction rate (k), and (d) •OH production rates for both $Fe_{78}Si_9B_{13}$ and $Fe_{73.5}Si_{13.5}B_9Cu_1Nb_3$ ribbons (pH 3.4, irradiation intensity: 7.7 μW/cm², dye concentration: 20 ppm, and H_2O_2 concentration: 1.0 mM).

Table 2
The comparable results of the production rates of •OH ($V_{•OH}$) by using various Fe-based catalysts.

Catalysts	Probe	H_2O_2 Concentration (mM)	pH	Light (μW/cm²)	$k_{•OH}$ (s^{-1})	Ref.
α-Fe_2O_3	Formic acid	12.0	4.0	–	4.0×10^{-7}	[45]
α-FeOOH	Formic acid	5.0	4.0	–	4.2×10^{-5}	[45]
$Fe_5HO_8 \cdot 4H_2O$	Formic acid	–	4.0	–	2.0×10^{-5}	[45]
FeOCl	Benzoic acid	15.6	–	–	2.9×10^{-4}	[46]
AA/Fe@Fe_2O_3	Benzoic acid	1.0	3.8	–	6.8×10^{-3}	[44]
Amorphous $Fe_{78}Si_9B_{13}$	Benzoic acid	1.0	3.4	7.7	5.7×10^{-2}	This work
Amorphous $Fe_{73.5}Si_{13.5}B_9Cu_1Nb_3$	Benzoic acid	1.0	3.4	7.7	3.3×10^{-2}	This work

This result indicates that the primary active species •OH are quickly quenched, causing a dramatic reduction in the amount available for further mineralizing the MB and MO dyes [3,43]. For better understanding the superior ability of $Fe_{78}Si_9B_{13}$ and $Fe_{73.5}Si_{13.5}B_9Cu_1Nb_3$ ribbons in dye degradation, the production rates of •OH ($V_{•OH}$) by use of benzoic acid (BA) as the probe [44,45] are shown in Fig. 3(d) and the corresponding data is summarized in Table 2. BA is rapidly oxidized by the •OH following with the pseudo-first-order kinetics (Eq. (6))

$$-\frac{d_{probe}}{d_t} = k_{probe} [probe] \tag{6}$$

where k_{probe} is the first kinetic constant (S^{-1}) and also can be described as the second-order kinetic rate for $V_{•OH}$, presenting in Eq. (7),

$$V_{•OH} = Scavenging \ rate = k_{•OH,p} [BA] [•OH] + \sum k_{OH,i} [S_i] [•OH] \tag{7}$$

where S_i presents •OH sink i in solution. Because the concentration ratio of the probe (BA) and H_2O_2 are employed for more than 1000 ($[BA]/[H_2O_2] > 1000$), the other scavenging effects (S_i) are ruled out as shown in Eq. (8),

$$V_{•OH} = k_{•OH,p} [BA] [•OH] \tag{8}$$

then the production rate of •OH ($V_{•OH}$) can be presented in Eq. (9)

$$V_{•OH} = k_{•OH} [H_2O_2] \tag{9}$$

where $[H_2O_2]$ is the H_2O_2 concentration, the corresponding data is plotted in Fig. 3(d).

As seen from Fig. 3(d) and Table 2, the •OH production rates ($k_{•OH}$) by using $Fe_{78}Si_9B_{13}$ and $Fe_{73.5}Si_{13.5}B_9Cu_1Nb_3$ are much faster than other Fe-based catalysts, indicating a superior dye degradation efficiency which is in good agreement with aforementioned. The likely explanation is that, 1) the short-range ordered and
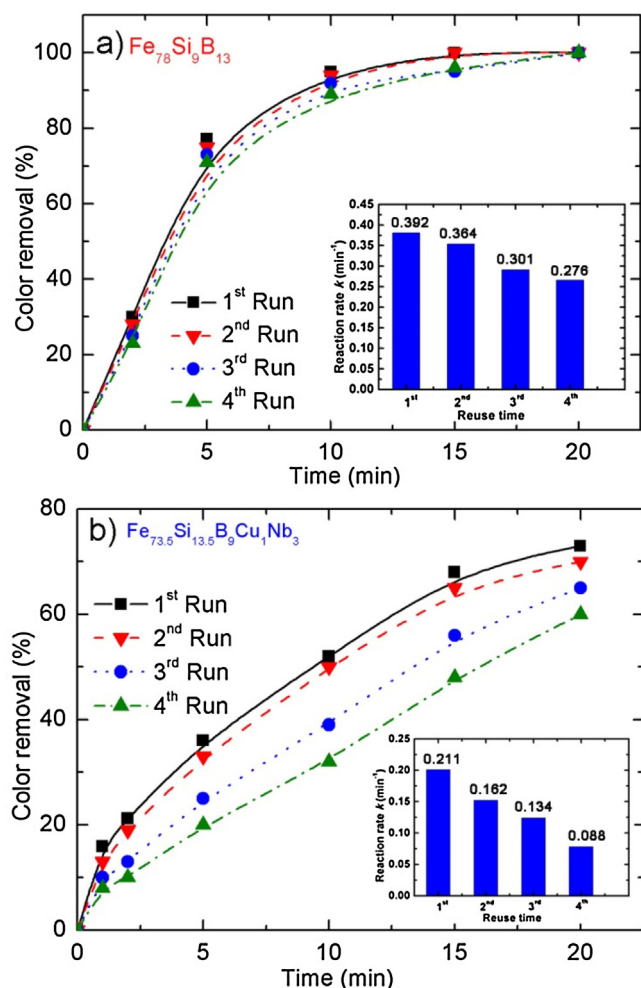
Fig. 4. Photo-enhanced Fenton-like degradation of MB dye with reused (a) $Fe_{78}Si_9B_{13}$ and (b) $Fe_{73.5}Si_{13.5}B_9Cu_1Nb_3$ amorphous alloys. Insets show the corresponding reaction kinetics (k) at various reused times.

long-range disordered atomic structure (weak atomic bonding) in amorphous alloy would cause easier electron activation under UV–vis light irradiation compared to the crystallized structure (metallic bonding in atoms); 2) the enhancement of Fe^{2+} being converted from Fe^{3+} under UV–vis light irradiation.

3.1.3. Reusability

Fig. 4 presents the multiple MB dye (pH 2) degradation cycles when using the same dosage of $Fe_{78}Si_9B_{13}$ and $Fe_{73.5}Si_{13.5}B_9Cu_1Nb_3$ ribbons in order to compare the efficiency of the color removal. As seen from Fig. 4(a) and inset, the color removal and reaction rates (k) slightly decrease when reusing $Fe_{78}Si_9B_{13}$ ribbons. After 20 min of irradiation, 100% color removal is achieved for all the recycled $Fe_{78}Si_9B_{13}$ ribbons. In contrast, it can be seen from Fig. 4(b), that the $Fe_{73.5}Si_{13.5}B_9Cu_1Nb_3$ ribbon shows only 60–70% color removal after 20 min irradiation for all the reused ribbons, the reaction rates (k) of the reused $Fe_{73.5}Si_{13.5}B_9Cu_1Nb_3$ ribbons show much slower efficiency when compared to the reused $Fe_{78}Si_9B_{13}$ ribbons. It is observed that the reaction rates (k) for both 1st run $Fe_{78}Si_9B_{13}$ and $Fe_{73.5}Si_{13.5}B_9Cu_1Nb_3$ ribbons present a rapid dye degradation efficiency: $k = 0.392\,min^{-1}$ of $Fe_{78}Si_9B_{13}$ and $k = 0.211\,min^{-1}$ of $Fe_{73.5}Si_{13.5}B_9Cu_1Nb_3$, indicating that these two as-received catalysts have an excellent dye degradation capability. In addition, it is interesting to observe that a sharp decrease in the reaction rate (k) for $Fe_{73.5}Si_{13.5}B_9Cu_1Nb_3$ ribbon starts from the 2nd run, from $0.211\,min^{-1}$ of the 1st run to $0.162\,min^{-1}$ of 2nd run and

down further to $0.088\,min^{-1}$ of 4th run. In contrast, the reaction rate (k) of $Fe_{78}Si_9B_{13}$ ribbon presents relatively stable behaviour from $k = 0.392\,min^{-1}$ for the 1st run to $k = 0.364\,min^{-1}$ for the 2nd run, while even the 4th run still shows the rapid reaction rate (k) of $0.276\,min^{-1}$. The reason for the difference in reaction rates (k) between $Fe_{78}Si_9B_{13}$ and $Fe_{73.5}Si_{13.5}B_9Cu_1Nb_3$ ribbons is that different precipitations are formed on the surface of the recycled $Fe_{78}Si_9B_{13}$ and $Fe_{73.5}Si_{13.5}B_9Cu_1Nb_3$ ribbons. The inclusion of niobium (Nb) in the $Fe_{73.5}Si_{13.5}B_9Cu_1Nb_3$ ribbon results in the niobium oxide precipitating onto the ribbon surface, which has a higher stability [47] compared to the precipitated SiO_2 on the $Fe_{78}Si_9B_{13}$ surface [3]. Consequently, the contacted area of Fe and H_2O_2 is reduced by the formed niobium oxide, thereby resulting in a decrease of the dye degradation reaction rate. For further study the surface aging behaviour, the effect of surface precipitation on the dye degradation efficiency of both $Fe_{78}Si_9B_{13}$ and $Fe_{73.5}Si_{13.5}B_9Cu_1Nb_3$ ribbons is presented in Section 3.2.

3.2. Characterizations

Fig. 5 shows the visual effect of surface decay on the reused $Fe_{78}Si_9B_{13}$ and $Fe_{73.5}Si_{13.5}B_9Cu_1Nb_3$ ribbons during dye degradation under simulated solar light. It can be seen that the as-received ribbon surfaces of both $Fe_{78}Si_9B_{13}$ and $Fe_{73.5}Si_{13.5}B_9Cu_1Nb_3$ are very smooth and present silver in color. As seen from Fig. 5(a), the reused $Fe_{78}Si_9B_{13}$ ribbon surface presents a rapid decay with an apparent color change from silver to yellow and finally to dark yellow. The corrosion holes start to be formed after the 3rd run. In contrast, the $Fe_{73.5}Si_{13.5}B_9Cu_1Nb_3$ ribbon surface shows a relatively slow decay, presenting a color change from silver to blue edges after the 1st run, followed with a combination of blue and light grey after the 3rd run, and finally to absolutely light grey. The yellow or dark yellow color on $Fe_{78}Si_9B_{13}$ ribbon surface indicates that the formed products are certain to include iron oxides; while the blue and light grey areas on $Fe_{73.5}Si_{13.5}B_9Cu_1Nb_3$ ribbon surface are postulated to be copper and niobium oxides, respectively. In order to confirm the formed precipitations on the surfaces of the $Fe_{78}Si_9B_{13}$ and $Fe_{73.5}Si_{13.5}B_9Cu_1Nb_3$ ribbon, the regions in Fig. 5 are selected for further characterizations in Fig. 6 and Fig. 7.

Fig. 6 shows the surface morphologies of the selected areas for the as-received and 3 times reused $Fe_{78}Si_9B_{13}$ ribbons in Fig. 5(a), respectively. As seen from Fig. 6(a) and (b), the as-received $Fe_{78}Si_9B_{13}$ ribbon surface is smooth with an atomic percentage of Fe (89.56%) to Si (10.44%). This value is very close to the nominal atomic ratio in the as-received $Fe_{78}Si_9B_{13}$ ribbon (78:9) when neglecting the undetected B element. Fig. 6(c) and (d) show the surface morphology and the corresponding EDS result of the 3rd time reused $Fe_{78}Si_9B_{13}$ ribbon. The elemental distributions of Fe, Si, and O are shown in Fig. 6(e–g). It is found that the amounts of Fe and Si reduce sharply after being reused 3 times under light irradiation while the amounts of S and O increase dramatically (the existence of S is not shown on the as-received $Fe_{78}Si_9B_{13}$ ribbon in Fig. 6 (b)). Fe is gradually consumed for the generation of •OH, which in turn causes an efficient degradation of the dye molecules. On the other side, the produced SiO_2 layer on the ribbon surface expanded strongly to provide stable protection for the buried Fe, which can significantly reduce the leaching efficiency of iron ions in the treated dye solution to further prevent the secondary pollution. The SiO_2 can easily be shaken off from the surface by stirring the dye solution to supply the maximum contact area between the buried Fe and H_2O_2 molecules, providing adequate •OH for dye molecules decomposition. As seen from Fig. 8(e), the troughs have a higher Fe concentration compared to other areas, which is confirmed to be the regions where SiO_2 has been previously deposited and afterward removed by stirring [3]. In addition, it is also important to note
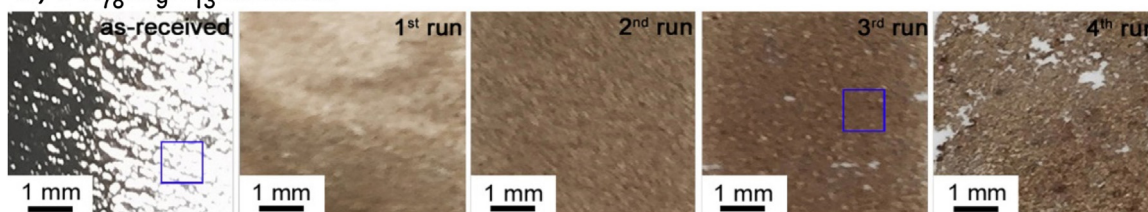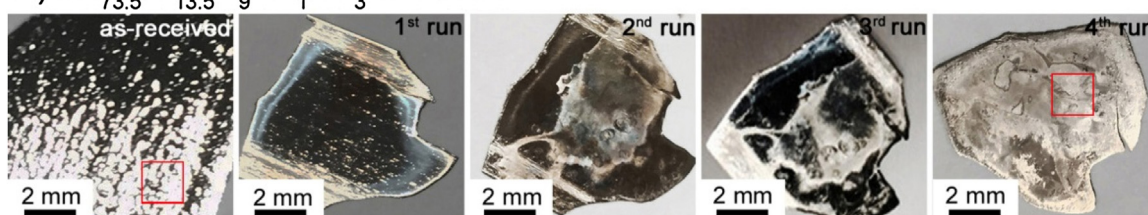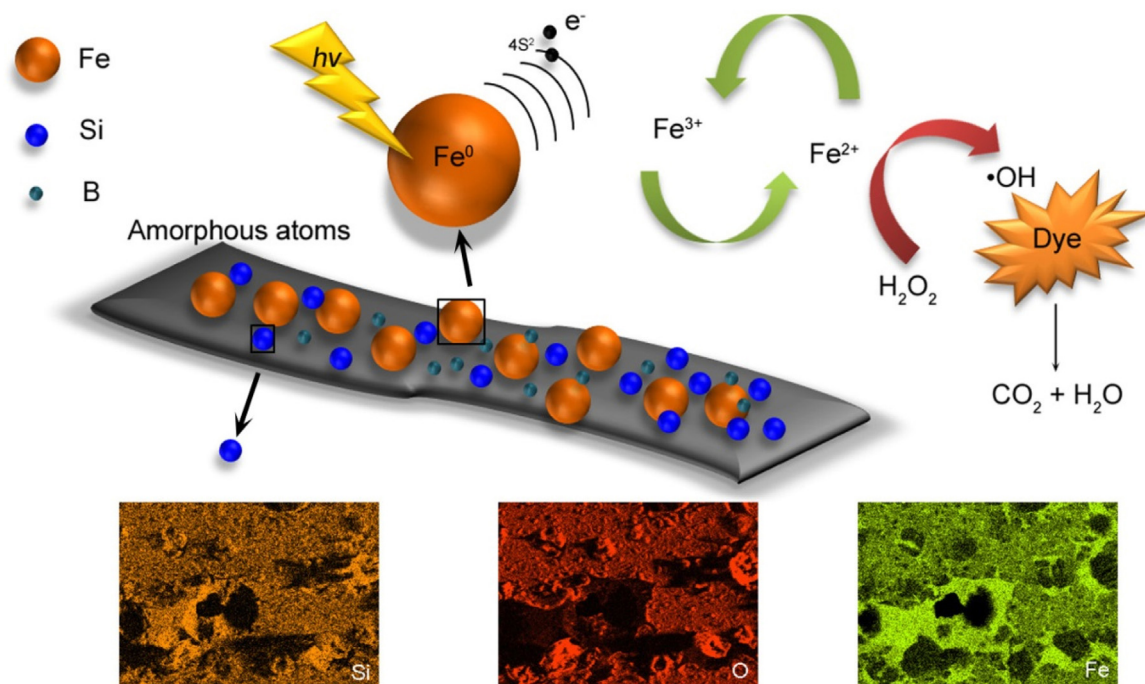
Fig. 5. Visual effect of ribbon surface change for the reused (a) $Fe_{78}Si_9B_{13}$ and (b) $Fe_{73.5}Si_{13.5}B_9Cu_1Nb_3$ catalysts during dye degradation under simulated solar light.

**Scheme 1.** The mechanism of dye degradation by using amorphous $Fe_{78}Si_9B_{13}$ alloy and the functionality of Fe, Si and B on surface aging behaviour under the UV–vis light.

that the regions having a low Fe concentration (protruding regions in Fig. 6(c, f, g)) are largely in the form of SiO_2 deposits, providing significant protection of the Fe on the ribbon surface. To summarize, the surface aging behaviour of the $Fe_{78}Si_9B_{13}$ ribbon during dye degradation can be expressed as follows: the isolated Fe atoms are consumed with H_2O_2 to produce the $^\bullet OH$ for the degradation of dye molecules. In the meantime, the SiO_2 layer is gradually expanded on the ribbon surface to protect the buried Fe. Subsequently SiO_2 is removed (by stirring) to ensure a great reaction area between the Fe and H_2O_2. Finally, along with the consumption of the Fe and Si, the ribbon surface continues to decay until it is corroded as holes.

Fig. 7(a) and (b) present the SEM image and EDS result of the as-received $Fe_{73.5}Si_{13.5}B_9Cu_1Nb_3$ ribbon. It is observed that the free surface is nearly smooth with initial atomic percentages of Fe (72.6%), Si (19.3%), Cu (0.4%), Nb (7.7%), having a close value with the nominal elemental ratio of $Fe_{73.5}Si_{13.5}B_9Cu_1Nb_3$

ribbon (B is not detectable). Fig. 7(c–h) shows the SEM image, the EDS and the Fe, Si, Cu, and Nb atomic distribution of the 4 times reused $Fe_{73.5}Si_{13.5}B_9Cu_1Nb_3$ ribbon. It is observed that these four elements are distributed homogeneously over the surface of the reused ribbon, indicating that $Fe_{73.5}Si_{13.5}B_9Cu_1Nb_3$ ribbon reacts uniformly with MB dye without significant compositional alteration after being reused 4 times. This result shows a different surface corrosive behaviour compared to the reused $Fe_{78}Si_9B_{13}$ ribbons. It is mainly attributed to the inclusion of Nb in the $Fe_{73.5}Si_{13.5}B_9Cu_1Nb_3$ alloy [47]. During the dye degradation reaction, niobium oxides are gradually formed on the ribbon surface overlapping the buried Fe. However, the niobium oxides are more stable than the precipitated SiO_2 on the reused $Fe_{78}Si_9B_{13}$ ribbons, resulting in the niobium oxides are more difficult to be removed by stirring. The formed niobium oxides overlay the surface of $Fe_{73.5}Si_{13.5}B_9Cu_1Nb_3$ ribbon thereby preventing the
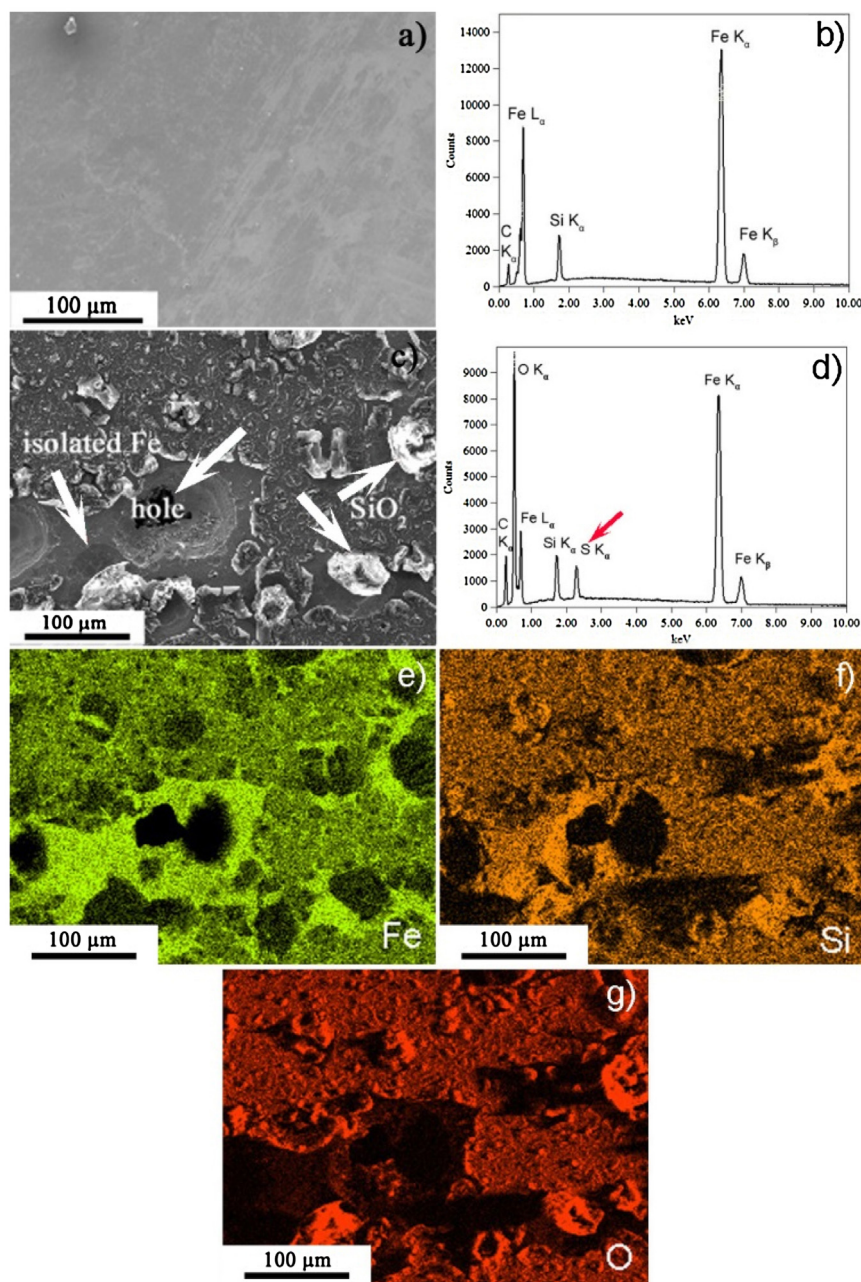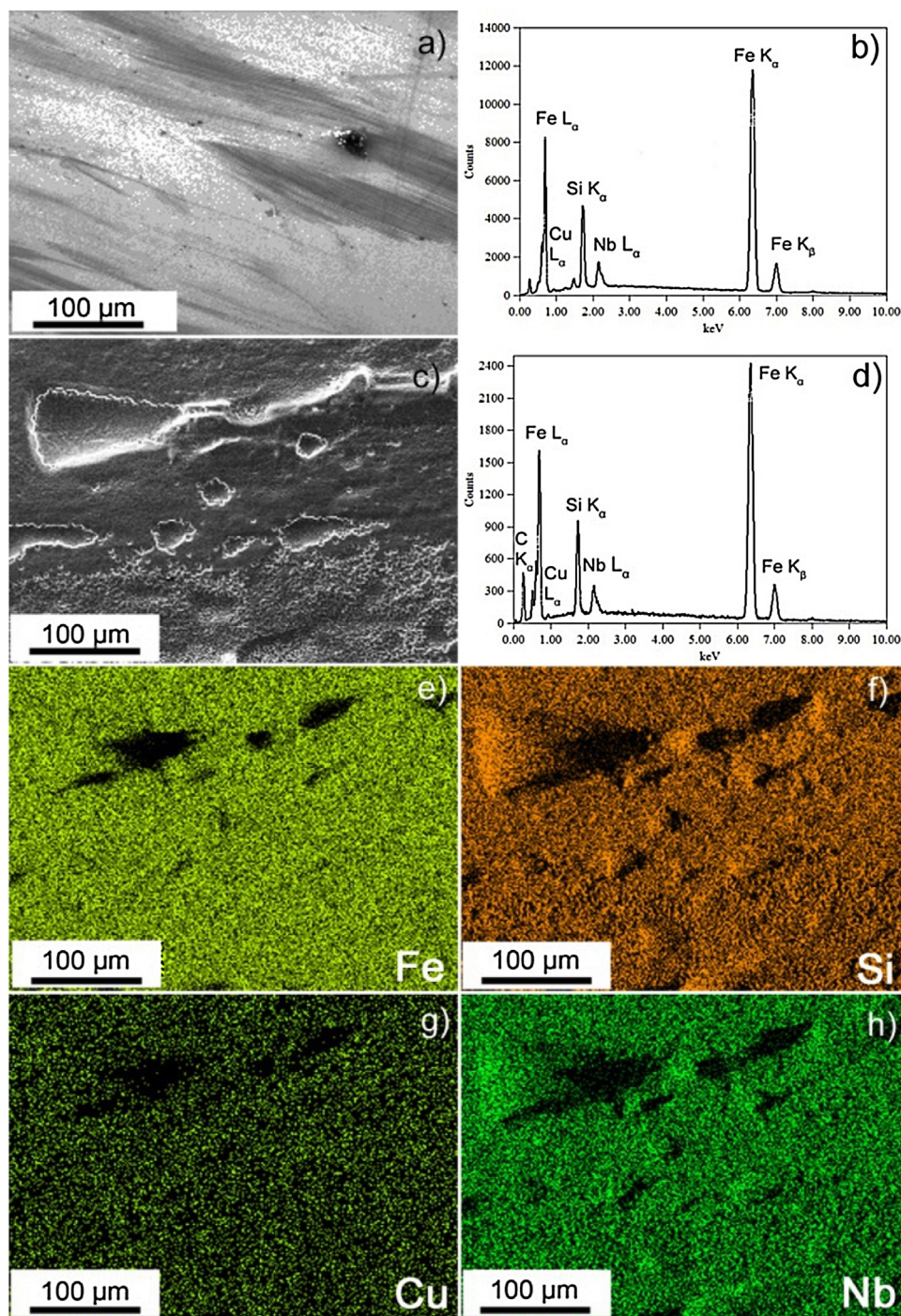
Fig. 6. (a) SEM image and (b) EDS analysis of as-received $Fe_{78}Si_9B_{13}$ ribbons, (c) SEM image, (d) EDS result, and (e) − (h) mapping results of 4th run recycled $Fe_{78}Si_9B_{13}$ ribbons.

reaction between Fe and H_2O_2. This explains why the reused $Fe_{73.5}Si_{13.5}B_9Cu_1Nb_3$ ribbon has a much slower dye degradation efficiency compared to the $Fe_{78}Si_9B_{13}$ ribbon. In addition, as seen in Fig. 6(c) and Fig. 7(c), the sulfur (S) element is also detected on the reused $Fe_{78}Si_9B_{13}$ ribbon surface whereas no S element is detected on the reused $Fe_{73.5}Si_{13.5}B_9Cu_1Nb_3$ ribbons. This result evidences that $Fe_{78}Si_9B_{13}$ ribbon has a greater adsorption ability than $Fe_{73.5}Si_{13.5}B_9Cu_1Nb_3$ ribbon. Due to the dye degradation using amorphous ribbons are based on the surface-reaction, stronger adsorption ability of $Fe_{78}Si_9B_{13}$ would provide the more contacted area between the produced $^\bullet$OH (only existing in nano-seconds) and dye molecules, further revealing the faster dye degradation of $Fe_{78}Si_9B_{13}$ compared to $Fe_{73.5}Si_{13.5}B_9Cu_1Nb_3$.

The Fenton-like dye degradation efficiency when reusing $Fe_{78}Si_9B_{13}$ and $Fe_{73.5}Si_{13.5}B_9Cu_1Nb_3$ ribbons is strongly influenced

by the presence and type of surface precipitation. Fig. 8 shows the XRD and UV–vis DRS characterizations of the as-received and 4th run recycled $Fe_{78}Si_9B_{13}$ and $Fe_{73.5}Si_{13.5}B_9Cu_1Nb_3$ ribbons. It is observed that both of the ribbon samples exhibit a broad diffuse diffraction peak (Fig. 8(a)), indicating that the structures of the as-received and recycled ribbons are basically in an amorphous state [36,37,48–51]. For both $Fe_{78}Si_9B_{13}$ and $Fe_{73.5}Si_{13.5}B_9Cu_1Nb_3$ ribbons after being 4 times used, the diffraction peaks ($2\theta_{max}$) present a higher intensity compared with the as-received $Fe_{78}Si_9B_{13}$ and $Fe_{73.5}Si_{13.5}B_9Cu_1Nb_3$ ribbons. Such comparatively higher intensity indicates that crystallized α-Fe is precipitated on the surface of both reused $Fe_{78}Si_9B_{13}$ and $Fe_{73.5}Si_{13.5}B_9Cu_1Nb_3$ ribbons during the dye degradation [3]. In addition, it is also interesting to note that the maximum diffraction peaks ($2\theta_{max}$) of the as-received $Fe_{78}Si_9B_{13}$ ribbon have only a miniscale difference in comparison

**Fig. 7.** (a) SEM image and (b) EDS analysis of as-received $Fe_{73.5}Si_{13.5}B_9Cu_1Nb_3$ ribbons, (c) SEM image, (d) EDS result, and (e) − (h) EDS mapping results of 4th run recycled $Fe_{73.5}Si_{13.5}B_9Cu_1Nb_3$ ribbons.

with the as-received $Fe_{73.5}Si_{13.5}B_9Cu_1Nb_3$ ribbon, *i.e.* $2\theta_{max} = 52.68°$ of $Fe_{78}Si_9B_{13}$ and $2\theta_{max} = 51.49°$ of $Fe_{73.5}Si_{13.5}B_9Cu_1Nb_3$, respectively. The adjacent atoms distance (*d*-space) of both amorphous $Fe_{78}Si_9B_{13}$ and $Fe_{73.5}Si_{13.5}B_9Cu_1Nb_3$ alloys can be calculated by Eqs. (10) and (11). It is noted that the calculated *d*-space of the as-received $Fe_{78}Si_9B_{13}$ ribbon is 0.2472 nm compared to the *d*-space of 0.2525 nm for $Fe_{73.5}Si_{13.5}B_9Cu_1Nb_3$ ribbon. The smaller *d*-space indicates that the $Fe_{78}Si_9B_{13}$ ribbon has a more compact atomic arrangement in the alloy, resulting in a relative lower free energy and further reducing dye degradation reactivity [52]. However, the inclusion of Nb in the $Fe_{73.5}Si_{13.5}B_9Cu_1Nb_3$ alloy enhances the sur-

face stability (Fig. 7). The results of the dye degradation efficiency of the reused $Fe_{78}Si_9B_{13}$ and $Fe_{73.5}Si_{13.5}B_9Cu_1Nb_3$ ribbons are shown in Fig. 4. It is confirmed that the poor performance of the reused $Fe_{73.5}Si_{13.5}B_9Cu_1Nb_3$ ribbons is because of the formation of niobium oxide on the surface, which tends to reduce the contact area between the Fe and H_2O_2, thereby decreasing the generation of $^{\bullet}$OH.

$$d = \frac{7.7}{k} \qquad (10)$$

$$k = \frac{4\pi sin\theta}{\lambda} \qquad (11)$$
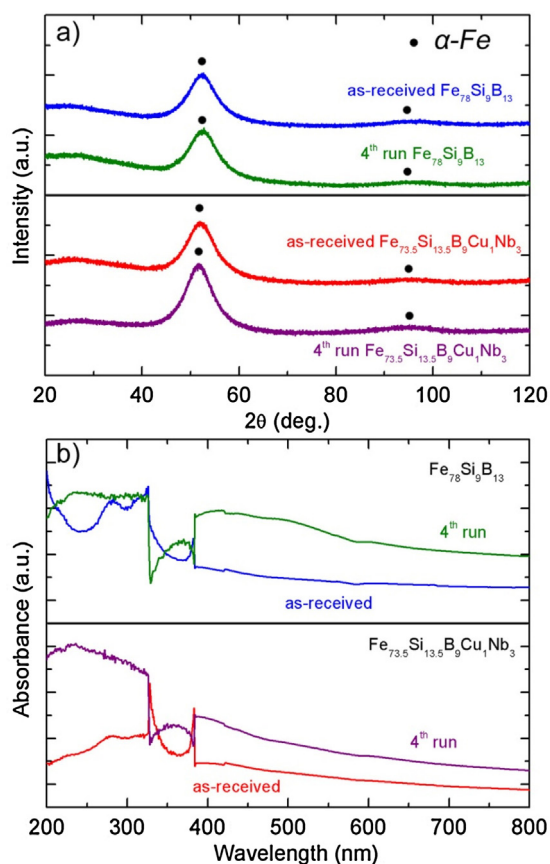
Fig. 8. (a) XRD characterization and (b) UV–vis DRS patterns of the as-received and recycled $Fe_{78}Si_9B_{13}$ and $Fe_{73.5}Si_{13.5}B_9Cu_1Nb_3$ ribbons (dye concentration: 20 ppm, pH 2, catalysts dosage: 0.5 g/L, H_2O_2 concentration: 1.0 mM, and irradiation intensity: 7.7 μW/cm).

where d is the adjacent atomic distance (d-space), λ is the wavelength of X-ray source used (Co-Kα: 0.179 nm).

The as-received and the 4th run recycled $Fe_{78}Si_9B_{13}$ and $Fe_{73.5}Si_{13.5}B_9Cu_1Nb_3$ ribbons are also characterized by UV–vis DRS (Fig. 8(b)). The bands between 200 and 300 nm indicate that the isolated iron species are homogeneously distributed on the ribbon surface, in either the tetrahedrally coordinated or octahedrally coordinated forms [53,54]. The bands in the range between 300 and 450 nm reflect the formation of $Fe^{3+}{}_xO_y$ complexes and those after 450 nm indicate the large iron oxide aggregates on the ribbon surface [53,54]. As seen from Fig. 8(b), the as-received $Fe_{78}Si_9B_{13}$ ribbon presents an obvious peak in the range between 200 and 300 nm, whereas the as-received $Fe_{73.5}Si_{13.5}B_9Cu_1Nb_3$ ribbon shows only a slight peak. It is confirmed that the isolated iron on the as-received $Fe_{78}Si_9B_{13}$ ribbon surface is more than that on the $Fe_{73.5}Si_{13.5}B_9Cu_1Nb_3$ ribbons, which is in good agreement with the nominal values expected for the $Fe_{78}Si_9B_{13}$ and $Fe_{73.5}Si_{13.5}B_9Cu_1Nb_3$ catalyst. For the range after 450 nm, there are no obvious peaks for either the as-received $Fe_{78}Si_9B_{13}$ or $Fe_{73.5}Si_{13.5}B_9Cu_1Nb_3$ ribbons, indicating that neither ribbon surfaces has iron oxides in the initial state. However, the 4th run reused $Fe_{78}Si_9B_{13}$ and $Fe_{73.5}Si_{13.5}B_9Cu_1Nb_3$ ribbons present significant peaks in the bands between 300 and 400 nm and even after 450 nm, indicating that a large amount of iron oxides are precipitated on the ribbon surface after they being reused.

Scheme 1 highlights the mechanism of dye degradation by using amorphous alloy and also demonstrates the functionality of Fe, Si and B on surface aging behaviour under the UV–vis light. According to the mechanism of Fenton reaction, the ferrous in the solution is the main source to react with H_2O_2 [55,56] rather than the solid zero-valent iron in the ribbon. The employed UV–vis light energy during the dye degradation significantly enhances the activation of the electrons on $4S^2$ orbital for the amorphous Fe atoms. In addition, the light energy also improves the Fe^{3+} to be converted back to Fe^{2+} for providing more concentration of the catalyst. The inclusion of Si and B [12] atoms in the amorphous alloy enhances the surface stability thereby improving the reusability.

4. Conclusion

The heterogeneous photo-Fenton-like MB and MO dye degradation efficiency of the reused $Fe_{78}Si_9B_{13}$ and $Fe_{73.5}Si_{13.5}B_9Cu_1Nb_3$ amorphous alloy ribbons was strongly influenced by the surface decay behaviour. It can be confirmed that the inclusion of Nb in the Fe-Si-B amorphous alloy improves the surface stability but reduces the reusability in terms of the dye degradation efficiency. In this work, the effects of pH, H_2O_2 concentration and light intensity on MB and MO dye degradation are investigated by employing $Fe_{78}Si_9B_{13}$ and $Fe_{73.5}Si_{13.5}B_9Cu_1Nb_3$ ribbons as the catalysts. In addition, it is found that the production rate of hydroxyl radicals ($\cdot$OH) by using amorphous alloy is 5–10 times faster than other Fe-based catalysts under light irradiation. The 1st run of $Fe_{78}Si_9B_{13}$ and $Fe_{73.5}Si_{13.5}B_9Cu_1Nb_3$ alloys has a fast dye degradation efficiency. However, a sharp decrease in the dye degradation efficiency occurred on the reused $Fe_{73.5}Si_{13.5}B_9Cu_1Nb_3$ alloys, whereas the $Fe_{78}Si_9B_{13}$ alloy shows a relatively stable value. The structural characterization reveals that the surface precipitations on the two alloys markedly affected their reusability in subsequent runs. The progress of the surface decay on the $Fe_{78}Si_9B_{13}$ ribbons begins with α-Fe, iron oxides and SiO_2 being precipitated on the surface. The surface then becomes corroded to the point where holes form at locations corresponding to the areas where the SiO_2 precipitate has fallen off the surface. In contrast, the niobium oxide precipitations on the $Fe_{73.5}Si_{13.5}B_9Cu_1Nb_3$ ribbon enhance the surface stability but sharply reduce the dye degradation efficiency.

In this study, a comparison of the surface precipitation morphology of $Fe_{78}Si_9B_{13}$ and $Fe_{73.5}Si_{13.5}B_9Cu_1Nb_3$ amorphous alloys has resulted in a significant advance in the understanding of catalyst decay. These findings have the potential to dramatically improve the cost-effectiveness and efficiency of catalysts and further enhance their stability and reusability when treating industrial wastewater.

References

[1] J. Schroers, G. Kumar, T.M. Hodges, S. Chan, T.R. Kyriakides, JOM 61 (2009) 21–29.
[2] H.F. Li, Y.F. Zheng, Acta Biomater. 36 (2016) 1–20.
[3] Z. Jia, W.C. Zhang, W.M. Wang, D. Habibi, L.C. Zhang, Appl. Catal. B: Environ. 192 (2016) 46–56.
[4] X.D. Qin, Z.W. Zhu, G. Liu, H.M. Fu, H.W. Zhang, A.M. Wang, H. Li, H.F. Zhang, Sci. Rep. 5 (2015) 18226.
[5] Y. Liu, J. Liu, S. Sohn, Y. Li, J.J. Cha, J. Schroers, Nat. Commun. 6 (2015) 7043.
[6] S. Parmanand, K. Neelam, K. Hisamichi, S. Yasunori, I. Akihisa, Nanotechnology 18 (2007) 035302.
[7] J.Q. Wang, Y.H. Liu, M.W. Chen, D.V. Louzguine Luzgin, A. Inoue, J.H. Perepezko, Sci. Rep. 2 (2012) 418.
[8] C. Zhang, Z. Zhu, H. Zhang, Z. Hu, J. Non-Cryst. Solids 358 (2012) 61–64.
[9] C.-C. Yang, X.-F. Bian, J.-F. Yang, Funct. Mater. Lett. 07 (2014) 1450028.
[10] C. Zhang, H. Zhang, M. Lv, Z. Hu, J. Alloys Compd. 356 (2010) 1703–1706.
[11] C. Zhang, Z. Zhu, H. Zhang, Z. Hu, Chin. Sci. Bull. 56 (2011) 3988–3992.
[12] Y. Tang, Y. Shao, N. Chen, K.-F. Yao, RSC Adv. 5 (2015) 6215–6221.
[13] X. Wang, Y. Pan, Z. Zhu, J. Wu, Chemosphere 117 (2014) 638–643.

[14] L. Sun, Y. Yao, L. Wang, Y. Mao, Z. Huang, D. Yao, W. Lu, W. Chen, Chem. Eng. J. 240 (2014) 413–419.
[15] S. Xie, P. Huang, J.J. Kruzic, X. Zeng, H. Qian, Sci. Rep. 6 (2016) 21947.
[16] Z. Jia, X. Duan, W.C. Zhang, W.M. Wang, H. Sun, S. Wang, C. Yang, L.C. Zhang, Sci. Rep. 6 (2016) 38520.
[17] Z. Jia, S.X. Liang, W.C. Zhang, W.M. Wang, C. Yang, L.C. Zhang, J. Taiwan Inst. Chem. Eng. (2017), http://dx.doi.org/10.1016/j.jtice.2016.11.021.
[18] P. Liu, J.L. Zhang, M.Q. Zha, C.H. Shek, ACS App. Mater. Interfaces 6 (2014) 5500–5505.
[19] A. Afkhami, M. Saber-Tehrani, H. Bagheri, Desalin 263 (2010) 240–248.
[20] J. Miao, L.C. Zhang, H.C. Lin, Chem. Eng. Sci. 87 (2013) 152–159.
[21] G. Mezohegyi, F. Gonçalves, J.J.M. Órfão, A. Fabregat, A. Fortuny, J. Font, C. Bengoa, F. Stuber, Appl. Catal. B: Environ. 94 (2010) 179–185.
[22] E. Guibal, J. Roussy, React. Funct. Polym. 67 (2007) 33–42.
[23] S. Karcher, A. Kornmuller, M. Jekel, Water Res. 36 (2002) 4717–4724.
[24] R. Saratale, G. Saratale, J. Chang, S. Govindwar, J. Taiwan Inst. Chem. Eng. 42 (2011) 138–157.
[25] J. Miao, Z. Jia, H.B. Lu, D. Habibi, L.C. Zhang, J. Taiwan Inst. Chem. Eng. 45 (2014) 1636–1641.
[26] Z. Jia, J. Miao, H.B. Lu, D. Habibi, W.C. Zhang, L.C. Zhang, J. Taiwan Inst. Chem. Eng. 60 (2016) 267–274.
[27] T. Wu, G. Liu, J. Zhao, H. Hidaka, N. Serpone, J. Phys. Chem. B 103 (1999) 4862–4867.
[28] Z. Bian, T. Tachikawa, P. Zhang, M. Fujitsuka, T. Majima, J. Am. Chem. Soc. 136 (2014) 458–465.
[29] I.A. Balcioglu, I. Arslan, Water Sci. Technol 43 (2001) 221–228.
[30] J.Q. Wang, Y.H. Liu, M.W. Chen, G.Q. Xie, D.V. Louzguine Luzgin, A. Inoue, J.H. Perepezko, Adv. Funct. Mater. 22 (2012) 2567–2570.
[31] C. Jiang, S. Pang, F. Ouyang, J. Ma, J. Jiang, J. Hazard. Mater. 174 (2010) 813–817.
[32] Y. Zhang, Z. Zhou, C. Chen, Y. Che, H. Ji, W. Ma, J. Zhang, D. Song, J. Zhao, ACS Appl. Mater. Interfaces 6 (2014) 12844–12851.
[33] P. Wardman, J. Phys. Chem. Ref. Data 18 (1989) 1637–1755.
[34] H. Katsumata, S. Kaneco, T. Suzuki, K. Ohta, Y. Yobiko, Chem. Eng. J. 108 (2005) 269–276.
[35] M.I. Pariente, F. Martínez, J.A. Melero, J.Á. Botas, T. Velegraki, N.P. Xekoukoulotakis, D. Mantzavinos, Appl. Catal. B: Environ. 85 (2008) 24–32.
[36] L.C. Zhang, J. Xu, J. Non-Cryst. Solids. 347 (2004) 166–172.
[37] H.B. Lu, L.C. Zhang, A. Gebert, L. Schultz, J. Alloys Compd. 462 (2008) 60–67.
[38] H.-Y. Shu, M.-C. Chang, H.-H. Yu, W.-H. Chen, J. Colloid Interface Sci. 314 (2007) 89–97.
[39] J. Fan, Y. Guo, J. Wang, M. Fan, J. Hazard. Mater. 166 (2009) 904–910.
[40] A. Baiker, Faraday Discuss. Chem. Soc. 87 (1989) 239–251.
[41] S. Nam, P.G. Tratnyek, Water Res. 34 (2000) 1837–1845.
[42] Y. Mu, H.-Q. Yu, S.-J. Zhang, J.-C. Zheng, J. Chem. Technol. Biotechnol. 79 (2004) 1429–1431.
[43] Y. Wang, H. Sun, X. Duan, H.M. Ang, M.O. Tadé, S. Wang, Appl. Catal. B: Environ. 172–173 (2015) 73–81.
[44] X. Hou, X. Huang, Z. Ai, J. Zhao, L. Zhang, J. Hazard. Mater. 310 (2016) 170–178.
[45] W.P. Kwan, B.M. Voelker, Environ. Sci. Technol. 37 (2003) 1150–1158.
[46] X.J. Yang, X.M. Xu, J. Xu, Y.F. Han, J. Am. Chem. Soc. 135 (2013) 16058–16061.
[47] N.A. Mariano, C.A.C. Souza, J.E. May, S.E. Kuri, Mater. Sci. Eng. A 354 (2003) 1–5.
[48] L.C. Zhang, Z.Q. Shen, J. Xu, Mater. Sci. Eng. A 394 (2005) 204–209.
[49] P. Yu, L.C. Zhang, W.Y. Zhang, J. Das, K.B. Kim, J. Eckert, Mater. Sci. Eng. A 444 (2007) 206–213.
[50] M. Calin, L.C. Zhang, J. Eckert, Scripta Mater. 57 (2007) 1101–1104.
[51] L.C. Zhang, K.B. Kim, P. Yu, W.Y. Zhang, U. Kunz, J. Eckert, J. Alloys Compd. 428 (2007) 157–163.
[52] J. Jayaraj, A. Gebert, L. Schultz, J. Alloys Compd. 479 (2009) 257–261.
[53] K. Sun, H. Xia, E. Hensen, R. van Santen, C. Li, J. Catal. 238 (2006) 186–195.
[54] J. Pérez-Ramírez, J. Catal. 227 (2004) 512–522.
[55] C. Liang, Y.-y. Guo, Environ. Sci. Technol. 44 (2010) 8203–8208.
[56] H. Kusic, I. Peternel, S. Ukic, N. Koprivanac, T. Bolanca, S. Papic, A.L. Bozic, Chem. Eng. J. 172 (2011) 109–121.